optica

Submicrometer-scale pattern generation via maskless digital photolithography

MINSU KANG,[1,2] CHANGHYUN HAN,[1,2] AND HEONSU JEON[1,2,3,*]

[1]Department of Physics and Astronomy, Seoul National University, Seoul 08826, Republic of Korea
[2]Inter-university Semiconductor Research Centre, Seoul National University, Seoul 08826, Republic of Korea
[3]Institute of Applied Physics, Seoul National University, Seoul 08826, Republic of Korea
*Corresponding author: hsjeon@snu.ac.kr

Received 24 August 2020; revised 19 November 2020; accepted 23 November 2020 (Doc. ID 406304); published 17 December 2020

Maskless photolithography based on digital micromirror devices (DMDs) is considered the next-generation low-cost lithographic technology. However, DMD-based digital photolithography has been implemented only for micrometer-scale pattern generation, whereas sophisticated photonic devices require feature sizes of approximately 100 nm. In this study, we adopt a high-magnification objective lens (200×) for a custom-built digital photolithography system to generate submicrometer-scale patterns. We also improvise techniques to augment the digital photolithography, pattern tilting, and grayscale exposure. We demonstrate that photonic crystal band-edge lasers of various lattice structures and periods can be quality-assessment testbeds.

https://doi.org/10.1364/OPTICA.406304

1. INTRODUCTION

Since its introduction, the digital micromirror device (DMD), a micro-optoelectromechanical system that enables digital light processing (DLP) technology, has been widely adopted for various applications [1], including the acclaimed DLP projectors used in modern projection displays, optical metrology [2], laser beam machining [3], etc. Maskless digital photolithography (MDPL) is an emerging technology that also utilizes DMDs [4]. In MDPL, patterns are dynamically controlled via spatial light modulator (or an *impromptu* photomask). The most common choice for spatial light modulator is DMD, where patterns can be conveniently reconfigured by electrically controlling light reflection from individual micromirrors. It becomes significantly advantageous because it requires no static photomask, thereby adding the convenience of '*masklessness*' to the existing merit of photolithography, high throughput. DMD had already substantially affected the sculpturing of microstructures in various dimensions—2D [5–8], 2.5D [9–16], and 3D [17–22]—and also studies on periodic structures [23–27], plasmonics [28], and bioapplications [29]. Therefore, MDPL might rapidly replace traditional photolithography, which requires masks. However, pattern sizes generated by MDPL so far are of micrometer scale, the smallest pattern demonstrated being 1.2 μm in period [26]. The fundamental resolution of an optical system, which is limited by *diffraction*, can be estimated using the Abbe's equation [30]: $d = \lambda/2n \sin\theta = \lambda/2\mathrm{NA}$, where d denotes the resolving power of the system, λ the wavelength of light, n the refractive index of the medium, and NA the numerical aperture of the lens. With a visible light source of moderate cost, the diffraction-limited pattern size is in the submicrometer range. Nonetheless, submicrometer-scale pattern generation via MDPL has been considered impractical, probably due to detrimental effects including non-monochromatism of the light source and interference among diffracted lights from individual micromirrors. This preconception has set 1 μm as a formidable task for MDPL, thereby hindering any systematic exploration for submicrometer pattern generation.

We report a systematic study on submicrometer-scale pattern generation using a custom-built MDPL system and its application potential. The combination of a DMD and high-magnification objective lens enabled us to generate photonic crystal (PhC) patterns with submicrometer lattice constants. To systematically assess the quality of the PhC patterns, we fabricated and evaluated PhC band-edge lasers (BELs), which are characterized by single-mode lasing action at a specific band-edge mode where the photon group velocity is null. To enhance the versatility of MDPL, we improvised two supplementary methods, *pattern tilting* and *grayscale exposure*. These methodological augmentations enabled us to fine-tune the PhC lattice constant on the scale of a few nanometers, and therefore, to control the BEL wavelength in a significantly finer step than those obtained using the standard MDPL procedure. The reduction of definable pattern size below 1 μm implies that MDPL finally advances into the territory of electron-beam lithography (EBL) (see Supplement 1, S1). Furthermore, the simultaneous pattern generation ability over a wide feature size range—from 10 μm down to the submicrometer level—in a single exposure shot can upscale photonics research and also facilitate the development of sophisticated photonic devices.

2. METHODS

A 50 nm thick, silicon-nitride hard mask layer was deposited on a commercially procured InGaAsP multiple-quantum-well (MQW) epilayer wafer via plasma-enhanced chemical vapor deposition (310PC, Surface Technology Systems) at the process temperature of 300°C. A positive photoresist (AZ MiR 701, MicroChemicals) was spin-coated on top of the hard mask layer to a thickness of 250 nm. The homemade MDPL system was employed to generate PhC patterns in the photoresist layer, with the exposure time below 10 s at the illumination intensity of ∼120 mW/cm^2. After pattern development using a photodeveloper (AZ 300 MIF, MicroChemicals), the patterns were sequentially transferred to the silicon-nitride hard mask layer and MQW layer via reactive-ion etching (RIE 80 Plus, Oxford Instrument). The photoresist and hard mask layers were then chemically removed. Finally, the 1 μm thick InP sacrificial layer under the MQW was selectively removed via HCl-based wet chemical etching to complete the air-bridge BEL device fabrication.

The emission spectra from the BEL devices were recorded using a homemade, fiber-based micro-photoluminescence (μPL) setup [31]. Notably, the setup employed a cleaved, butt-end fiber probe tip with the core diameter of 62.5 μm both for optical excitation and emitted-light collection. The fiber probe tip was brought close to the sample surface, while its other end was fused to a 1 × 2 fiber coupler. The input port of the coupler was connected to a 1064 nm pulsed laser diode (PSL10, Multiwave Photonics), which operated at a 500 kHz repetition rate with 20 ns pulse duration. The output port was connected to an optical spectrum analyzer (Q8381A, Advantest) for spectral analysis.

Numerical simulations, which were based on the FDTD method, were performed using a commercial software package (FDTD Solutions, Lumerical Solutions). For the band structure calculations, multiple dipole sources were randomly distributed in terms of their positions, polarization directions, and phases. Bloch boundary conditions were applied along the lateral directions, while the upper and lower boundaries of the simulation field were capped using perfectly matching layers. The spatial resolution was set to 41 pixels per μm. Throughout the simulations, we neglected the imaginary parts of the dielectric constants of the composing materials, assuming that the optical excitation occurs just above the lasing threshold so that the MQWs become optically transparent without any optical loss or gain.

3. DIGITAL PHOTOLITHOGRAPHY SYSTEM

Our MDPL system comprises a tube lens and a 200× objective lens (CF Plan Apo 200, Nikon; NA = 0.9), configured in a typical 4f optical system [32] to project the image reduced from DMD (DLP4710, Texas Instruments) onto the sample plane [see Fig. 1(a)]. The DMD used is a 1920 × 1080 array of

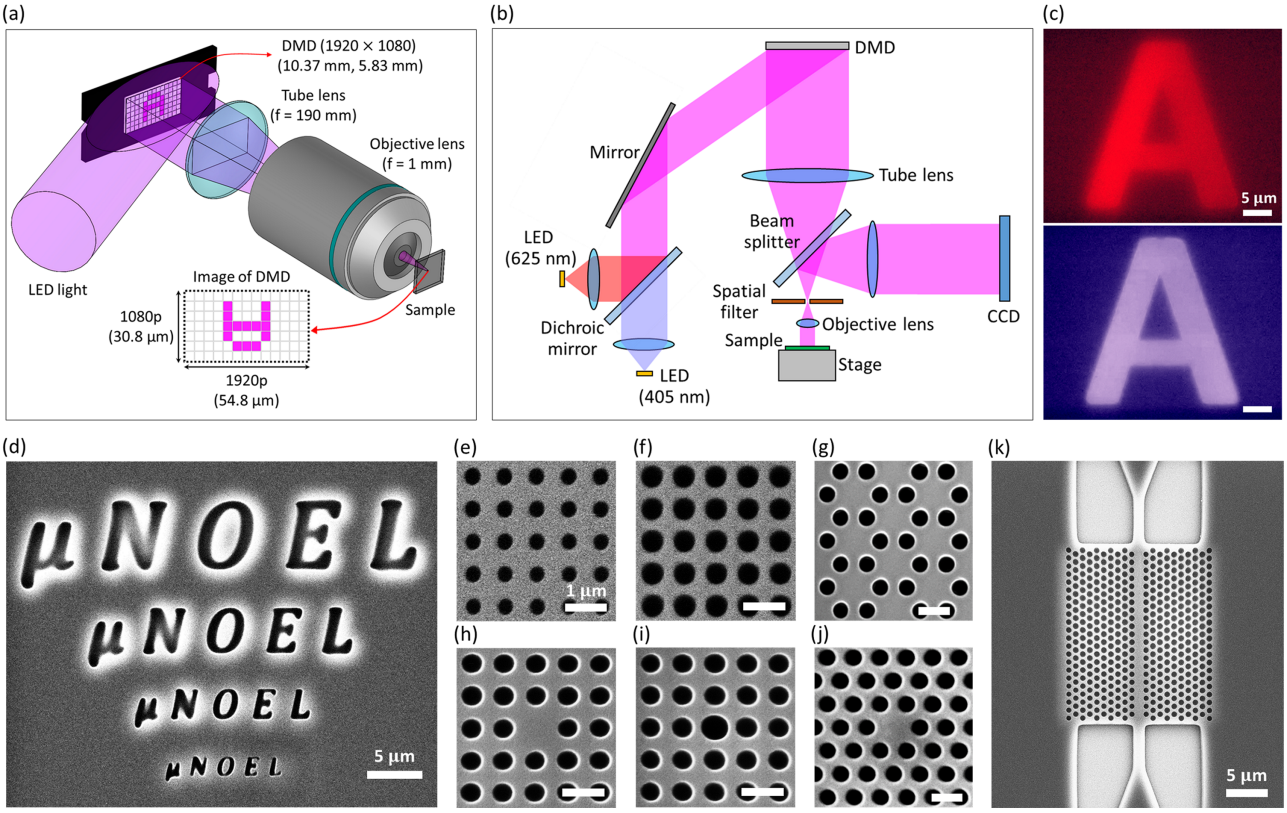

Fig. 1. Digital photolithography system. (a) Schematic of the MDPL system. The LED light, whose cross-sectional intensity profile is spatially modulated by the DMD, is demagnified by the combination of tube lens and objective lens, resulting in a reduced image formed on the sample plane. The size of the DMD image is 54.8 μm × 30.8 μm. (b) Two operation modes of the MDPL system. The focusing mode (λ = 625 nm; red) is to bring the image plane to the sample surface without triggering any photochemical reaction in photoresist. In the exposure mode (λ = 405 nm; violet), a DMD pattern is photochemically inscribed in the photoresist layer on the sample. The two modes share most of the optical path (magenta). (c) DMD images on the sample plane, captured by CCD camera in the two operation modes: focusing (top) and exposure (bottom). (d–k) SEM images of various photoresist patterns generated by the MDPL system: (d) μNOEL logos in different sizes, PhC patterns (e–g) without and (h–j) with a defect, and (k) a PhC waveguide joint with two conventional waveguides at both ends.

square micromirror pixels with the pitch P of 5.4 μm. The sizes of image (i) and object (o) are related by $i = o(f_2/f_1)$, where $f_1 (= 190$ mm) and $f_2 (= 1$ mm) denote the effective focal lengths of the tube lens and objective lens, respectively. The resulting image reduction ratio is $R = f_2/f_1 = 1/190$. The system is designed and built to operate in dual modes, as depicted in Fig. 1(b): the focusing and exposure modes. The focusing mode, which operates using a red light-emitting diode (LED) source ($\lambda = 625$ nm) and thus does not affect the photoresist, brings the DMD image plane right onto the sample surface. This procedure is indispensable to submicrometer feature generation, and also should be highly useful for pattern alignment when serial multiple exposures are required. In the subsequent exposure mode, the light source is switched to a violet LED ($\lambda = 405$ nm) to transfer the DMD pattern to the photoresist layer on the sample. Figure 1(c) depicts the color images of a marker pattern 'A' imaged on the sample plane during the two MDPL modes.

Although the simple theory based on ray optics suggests a high reduction ratio ($R = f_2/f_1 = 1/190$), and consequently a small DMD pixel image ($p = P \times R \approx 28.4$ nm), such a small pixel image significantly below 100 nm is highly impractical to be generated due to diffraction. Thus, we performed preliminary experiments to determine the resolving power of our system (see Supplement 1, S2), following which we obtained $d \approx 357$ nm, which is still substantially larger than the Abbe limit, $d \approx 225$ nm, implying room for further development. Figure 1(d) shows a scanning electron microscopy (SEM) image of a photoresist pattern on silicon substrate, where our laboratory logo is created multiple times in different sizes. The smallest pattern linewidth, which is the upper horizontal stroke of the bottommost letter 'E', is approximately 180 nm, roughly half the resolving power of our system. Figures 1(e)–1(j) show the PhC patterns of square, honeycomb, and hexagonal lattices, without (e–g) and with (h–j) a defect. Figure 1(k) shows a hybrid waveguide pattern generated by single exposure, where a PhC waveguide is joined together with two tapered conventional waveguides on both the ends.

4. SQUARE-LATTICE PHOTONIC CRYSTAL BAND-EDGE LASERS

To assess the quality of the submicrometer-scale patterns generated using our MDPL system, we fabricated PhC BELs in an air-bridge membrane [see Fig. 2(a)]. We began with square-lattice PhC structures because their lattice symmetry is similar to that of the DMD. A square-lattice PhC pattern (lattice constant $a = 714$ nm), which comprised an array of circular air-holes (radius $r = 0.35a$), was formed in an InGaAsP-based MQW epilayer (thickness $t = 230$ nm) that emits photons at $\lambda \approx 1550$ nm. The lattice constant was determined such that the optical gain band of the MQWs overlapped with the Γ_1 band-edge ($a/\lambda \approx 0.47$) [see Fig. 2(b)].

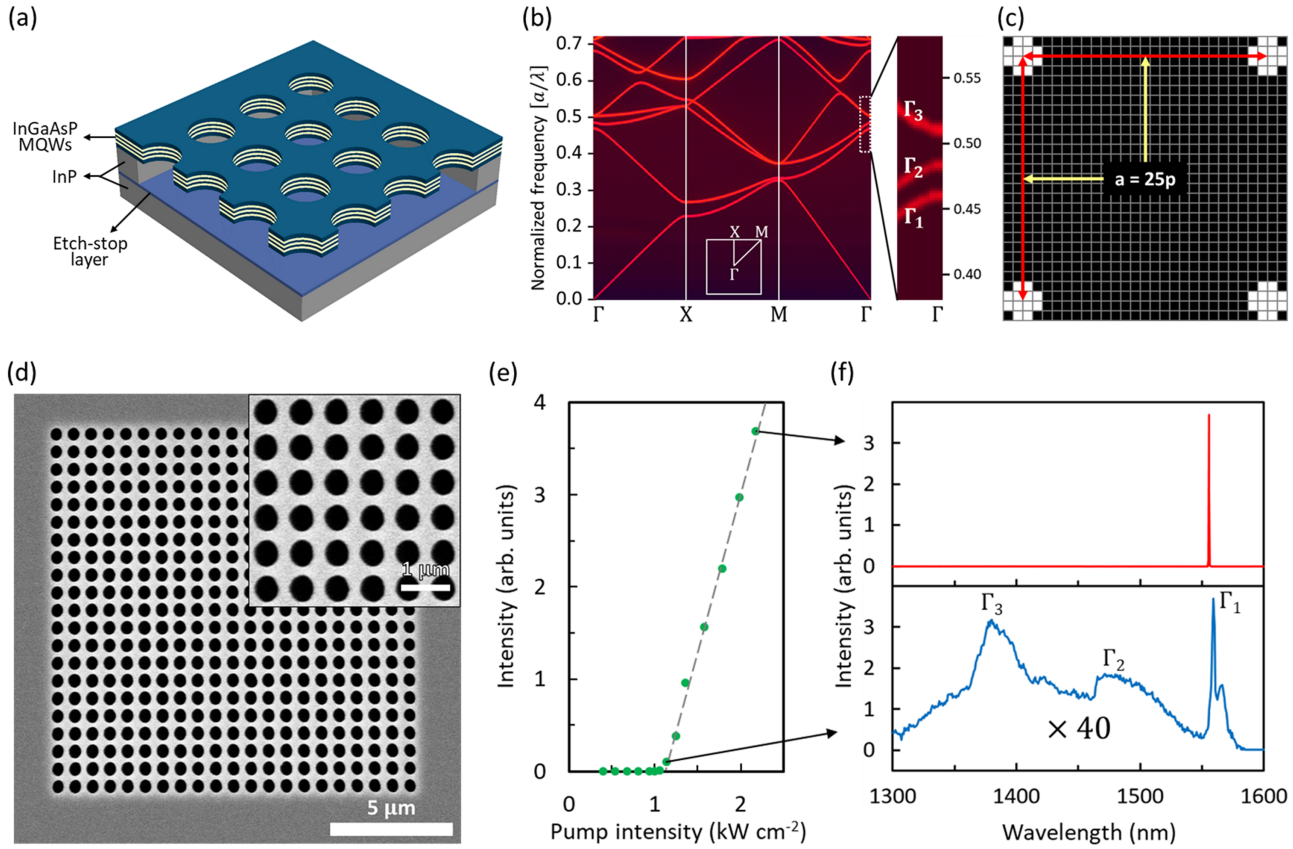

Fig. 2. Square lattice PhC BEL. (a) Schematic of the air-bridge square lattice PhC BEL device. (b) Photonic band structure calculated for the square lattice PhC slab waveguide: $a = 714$ nm, $r = 0.35a$, $t = 230$ nm. (c) DMD pixel layout for a unit cell of the square lattice PhC structure. The white and black squares represent the 'on' and 'off' states of the corresponding DMD micromirrors, respectively. The lattice constant, determined by the number of pixels between two adjacent hole pattern centers, is marked by the arrow-tipped red lines: $a = 25p \approx 714$ nm. (d) SEM image of a fabricated square lattice PhC BEL device. The inset is a higher-magnification image. (e) $L - L$ curve measured of an optically pumped BEL device. (f) Emission spectra measured above (top) and near (bottom) laser threshold.

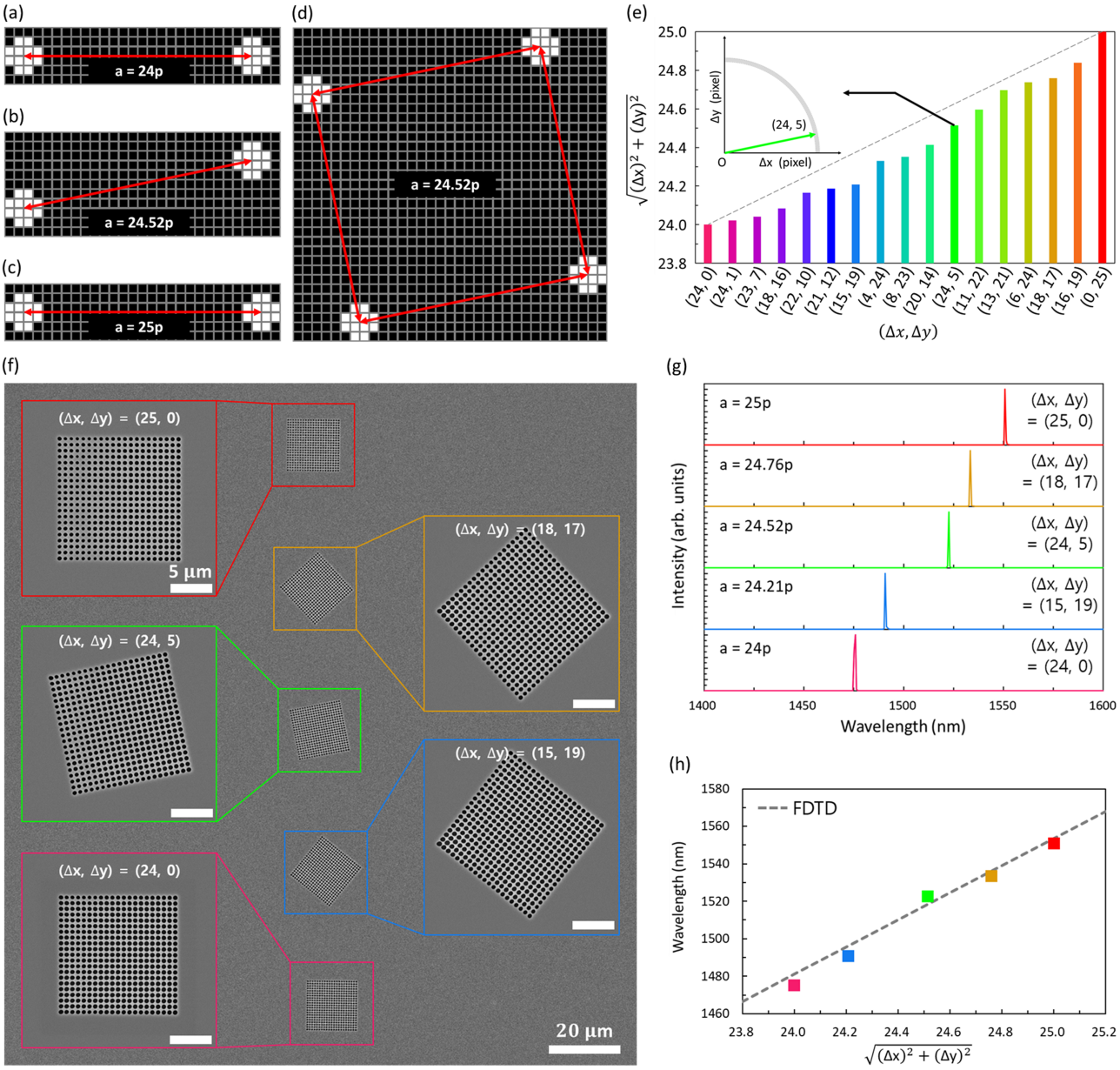

Fig. 3. Pattern tilting. (a–d) DMD pixel layouts to generate a lattice constant in between two sequential integer multiples of $a = 24p$ and $25p$ by pattern tilting. The white and black squares represent the 'on' and 'off' states of the corresponding DMD pixels, respectively. The lattice constants of the resultant PhCs are (a) $a = 24p$, (b) $\sim 24.52p$, and (c) $a = 25p$, while shown in (d) is a unit cell of the square lattice PhC having the lattice constant of (b). (e) 17 pattern-tilting configurations $(\Delta x,\ \Delta y)$ that result in the lattice constant of $24p \le a \le 25p$. The inset illustrates an example configuration of (24, 5). (f) SEM image of a fabricated device, which contains five square lattice PhC BEL devices in different tilting configurations: from top to bottom, (25, 0), (18, 17), (24, 5), (15, 19), and (24, 0). The insets are the magnified images of the five BEL devices. (g) μPL spectra (above threshold) measured from the five PhC BEL devices in (f). (h) Relationship between BEL lasing wavelength and PhC lattice constant.

The band structure calculations were performed based on the finite-difference time-domain (FDTD) method.

As depicted in Fig. 2(c), the lattice constant was selected to be 25 pixels ($a = 25p \approx 714.0$ nm), while each hole pattern was defined using a group of 12 DMD pixels, which are represented using the white pixels in the figure. The relationship between the DMD configuration for hole generation and the resultant hole pattern is explained in Supplement 1, S3. Figure 2(d) shows an SEM image of a fabricated square-lattice BEL device, which comprises an array of 21×21 air-holes in the MQW epilayer.

The fabricated BEL device was optically excited using a pulsed, 1064 nm laser diode (at 1% duty cycle). Figure 2(e) depicts a typical, light-in versus light-out ($L - L$) relationship, exhibiting sharp laser turn-on with a clear threshold at approximately 1.2 kW/cm^2, comparable to that of a similar BEL device that our group previously fabricated via EBL [33]. The μPL spectra above (top) and near (bottom) the threshold are depicted in Fig. 2(f). The spectrum near the threshold exhibits three distinct emission peaks, which correspond to the three Γ-point band-edges marked in Fig. 2(b). These experimental results indicate that MDPL is accurate and

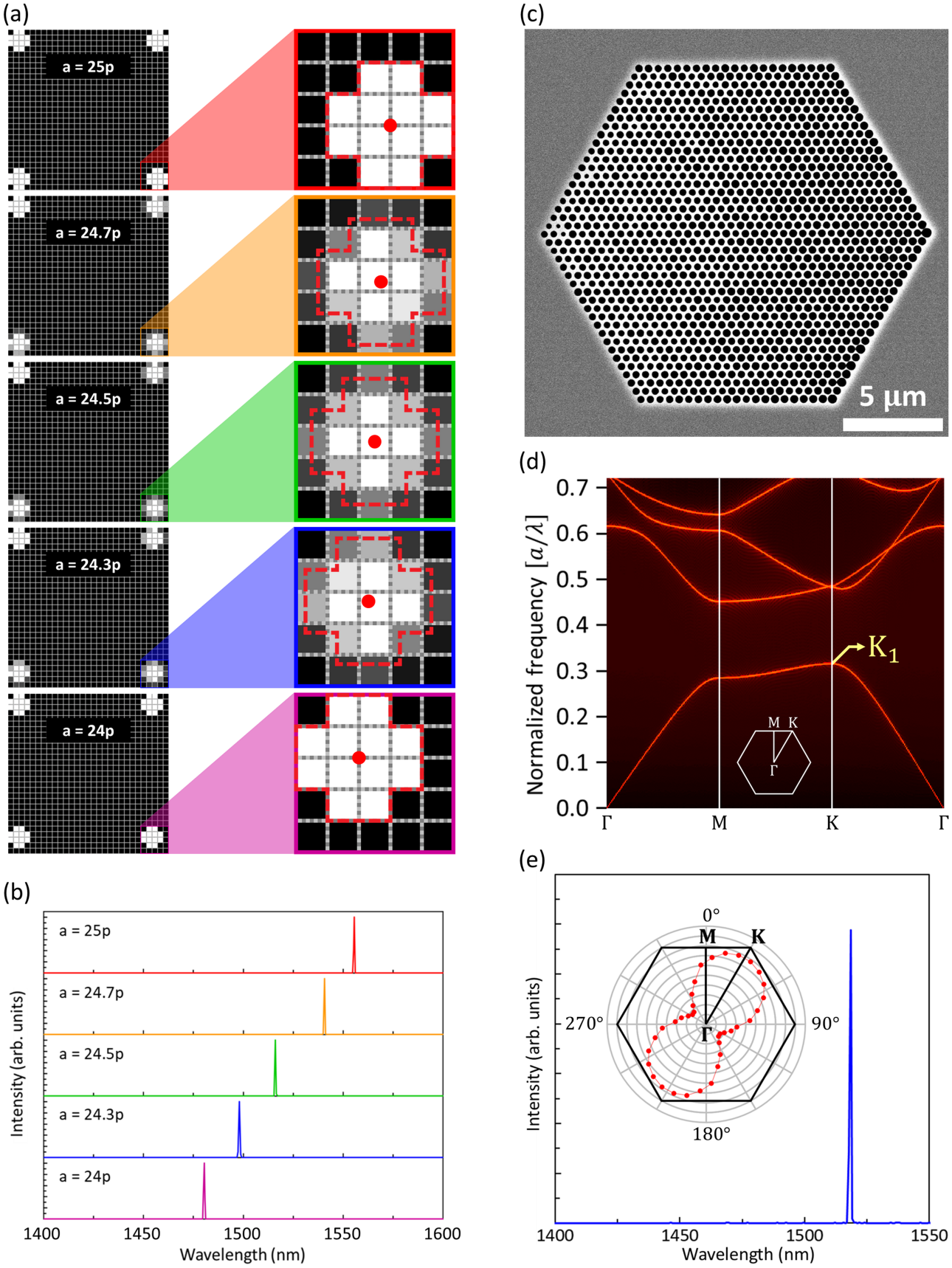

Fig. 4. Grayscale exposure. (a, b) Square lattice PhCs by the grayscale exposure. (a) DMD pixel layouts to generate fine-step lattice constants by the grayscale exposure. Shown in the right column are the enlarged 5 × 5 pixel areas at the bottom right corners of the DMD layouts in the left column. Outlined in the red dashed lines are the boundaries of intended hole patterns, while the red dots indicate the centers of the patterns. (b) μPL spectra (above threshold) measured from the BEL devices fabricated by the grayscale exposure method shown in (a). (c–e) Hexagonal lattice PhC BEL device fabricated by the grayscale exposure: (c) SEM image of the device, for which $a \approx 16.7p \approx 477$ nm, (d) calculated photonic band structure, and measured μPL spectrum. Inset in (e) shows the polarization dependence of the BEL emission.

sufficiently reliable to fabricate sophisticated photonic devices with submicrometer features.

5. FINE-TUNING THE LATTICE CONSTANT: PATTERN TILTING

Because of the digital nature of DMD, the lattice constant of a square-lattice PhC can only be discretely controlled; the finest step in the lattice constant corresponds to the size of a single DMD pixel image, which is $\Delta a = p = 28.4$ nm in our system. Notably, diffraction only limits the minimum feature size to be defined, not the distance between adjacent features. Therefore, employing a high-magnification objective lens is advantageous in terms of not only signifying the pattern reduction ratio (within the diffraction limit) but also enhancing the design flexibility. Nonetheless, the resultant BEL wavelengths attainable using our MDPL system are widely separated: $\Delta\lambda \approx 75$ nm for the Γ_1 band-edge mode when the lattice constant changes from $a = 24p$ to $25p$. This wavelength step is extremely cumbersome for meeting the requirements of sophisticated photonic device applications; for example, the channel spacing even in coarse wavelength division multiplexing is 20 nm [34]. Accordingly, we propose *pattern tilting* as a solution until the hardware for the required speculations becomes available.

Figures 3(a)–3(d) illustrate in the pixelated plane how to improvise the square-lattice PhC structure with an intermediate lattice constant by tilting patterns. The right hole, initially apart from the left one by 24 pixels [see Fig. 3(a)], is vertically shifted by 5 pixels [see Fig. 3(b)], and the shift is denoted by $(\Delta x, \Delta y) = (24, 5)$. The resultant hole-to-hole distance is given by $p\sqrt{(x)^2 + (y)^2} = p\sqrt{24^2 + 5^2} \approx 24.52p$, which is greater than $24p$ but smaller than $25p$ [see Fig. 3(c)]. By accordingly arranging the other hole patterns, we can generate a square-lattice PhC structure with a new lattice constant $a \approx 24.52p$ [see Fig. 3(d)]. Figure 3(e) displays all the possible tilting configurations that produce inter-hole distances between $24p$ and $25p$.

By excluding the redundant configurations due to the commutativity between Δx and Δy, as well as the four pairs of accidentally degenerate configurations—(23, 7) and (17, 17), (24, 2) and (18, 16), (24, 3) and (21, 12), and (23, 9) and (21, 13), we identify 17 inter-hole distances in the range of $24p \le a \le 25p$. The average step size in the lattice constant is $\Delta a = p/16 \approx 1.78$ nm, which is smaller by an order of magnitude than the step size obtained without pattern tilting ($\Delta a = p = 28.4$ nm).

To demonstrate the validity of the proposed idea, we fabricated a series of square-lattice PhC BELs using the pattern-tilting method. Figure 3(f) shows an SEM image of the square-lattice PhC BEL devices in five different tilting configurations, which are arranged in the decreasing order of lattice constant: (25, 0) (18, 17), (24, 5), (15, 19), and (24, 0) from top to bottom. Although one can scarcely notice the differences in lattice constant, one can certainly recognize the high quality of the PhC patterns irrespective of the tilt angles. Upon optical excitation, a single-mode BEL peak was spontaneously produced from each device. As shown in Fig. 3(g), the BEL wavelength shifted systematically and monotonically in response to the change in lattice constant. The lasing wavelength is plotted as a function of the PhC lattice constant in Fig. 3(h), and it agrees well with the FDTD simulation results. Similarly, the pattern-tilting method can be applied to a hexagonal PhC lattice, albeit with some limitations (see Supplement 1, S4).

6. FINE STRUCTURAL TUNING: GRAYSCALE EXPOSURE

There exists a more versatile method than pattern tilting to fine-tune MDPL patterns: *grayscale exposure*, in which the brightness of each DMD pixel is individually adjusted by means of its exposure time (see Supplement 1, S5). The grayscale exposure method enables not only the fine control of lattice constant but also the generation of arbitrary patterns, even those patterns that are incommensurate with the DMD pixel layout, such as a hexagonal PhC lattice, thereby significantly enhancing the design flexibility. Figure 4(a) depicts the manner in which grayscale exposure can generate square-lattice PhC patterns with arbitrary lattice constants ($24p \le a \le 25p$). The idea is to differentiate the exposure time for each pixel in proportion to the degree of the spatial overlap between the pixel and pattern to be generated. The patterns to be generated have been outlined using dashed red lines in the right column of Fig. 4(a), which depicts the enlarged 5×5 pixel areas in the bottom right corners of the corresponding DMD pixel layouts. Notably, pixel intensity is expressed in grayscale, not in the binary format of 'on (white)' or 'off (black)'. Accordingly, five square-lattice PhC BEL devices were fabricated. The resultant BEL devices were optically excited to induce lasing actions. As shown in Fig. 4(b), all the BEL devices exhibit single-mode lasing, while their spectral positions systematically shift towards the shorter wavelength as the PhC lattice constant decreases. The rate of the BEL wavelength shift is $\Delta\lambda/\Delta a \approx 2.63$ nm/nm, which agrees well with the theoretical calculation of $\Delta\lambda/\Delta a \approx 2.54$ nm/nm.

To demonstrate the versatility of the grayscale exposure method, we also fabricated hexagonal-lattice PhC structures. Notably, the hole positions in the hexagonal lattice are completely incommensurate with the DMD layout, in which micromirrors are arranged in square-lattice symmetry. As demonstrated in Fig. 4(c), a high-quality hexagonal-lattice PhC BEL device was realized using the grayscale exposure method. The lattice constant was selected such that the in-plane K_1 band-edge mode, which is indicated in Fig. 4(d), matched with the optical gain bandwidth. The resultant lasing spectrum is shown in Fig. 4(e), which clearly exhibits single-mode lasing, a characteristic feature of BEL. The polarization distribution measured for the BEL emission [inset of Fig. 4(e)] exhibits strong linear polarization along the K direction, thereby strongly indicating band-edge lasing action at the K-point. All these results indicate that, when combined with the grayscale exposure method, MDPL becomes a versatile and powerful photolithographic technique capable of generating submicrometer-scale PhC patterns of any lattice type and period.

7. DISCUSSION AND CONCLUSION

In summary, the well-known DMD is combined with a high-magnification objective lens to explore the limitations of digital photolithography in regard to the smallest feature size that can be defined. Although still diffraction-limited, the homemade MDPL system is proven to be capable of generating submicrometer-scale patterns of quality sufficiently high for sophisticated photonic device applications. The PhC BEL devices fabricated using the system exhibit stable single-mode lasing action at thresholds that are comparable to those of similar BELs fabricated via EBL. Two augmenting methods, pattern tilting and grayscale exposure, are also developed to overcome the weakness of the digital photolithography system. Both the methods enable pattern periods other

than the integer-multiples of the DMD pixel image size, thereby resulting in BELs with significantly fine wavelength channel spacing. By adopting a short-wavelength light source and an advanced photolithographic technique such as immersion lithography, even smaller features of arbitrary shapes or lattice symmetries can be generated. In addition to the hardware improvements, software modifications—including intensity correction for spatially uniform exposure [35], active compensation of optical aberration and diffraction [36–39], enhanced spatial resolution [40–42], and accelerated exposure speed [43,44]—may also improve the performance of the MDPL technology. Our results initiate the development of low-cost, high-throughput photolithographic equipment, which is appropriate for the low-volume manufacturing of sophisticated photonic devices that have stringent pattern requirements and may also replace existing nanofabrication techniques, such as EBL, that suffer from extremely low throughput.

Funding. National Research Foundation of Korea (NRF-2020R1A2C2008583).

Disclosures. The authors declare no conflicts of interest.

See Supplement 1 for supporting content.

REFERENCES

1. D. Dudley, W. Duncan, and J. Slaughter, "Emerging digital micromirror device (DMD) applications," Proc. SPIE **4985**, 14–26 (2003).
2. L. Zhang, Q. Chen, C. Zuo, and S. Feng, "Real-time high dynamic range 3D measurement using fringe projection," Opt. Express **28**, 24363–24378 (2020).
3. D. J. Heath, J. A. Grant-Jacob, Y. Xie, B. S. Mackay, J. A. G. Baker, R. W. Eason, and B. Mills, "Machine learning for 3D simulated visualization of laser machining," Opt. Express **26**, 21574–21584 (2018).
4. H. Martinsson, T. Sandstrom, A. Bleeker, and J. D. Hintersteiner, "Current status of optical maskless lithography," J. Microlith. Microfab. Microsyst. **4**, 011003 (2005).
5. Y. Liu, Y. Zhao, X. Dong, M. Zheng, F. Jin, J. Liu, X. Duan, and Z. Zhao, "Multi-scale structure patterning by digital-mask projective lithography with an alterable projective scaling system," AIP Adv. **8**, 065317 (2018).
6. R. C. Auyeung, H. Kim, S. Mathews, and A. Pique, "Spatially modulated laser pulses for printing electronics," Appl. Opt. **54**, F70–F77 (2015).
7. S. Wen, A. Bhaskar, and H. Zhang, "Scanning digital lithography providing high speed large area patterning with diffraction limited sub-micron resolution," J. Micromech. Microeng. **28**, 075011 (2018).
8. J. Kim and K. Jeong, "Batch fabrication of functional optical elements on a fiber facet using DMD based maskless lithography," Opt. Express **25**, 16854–16859 (2017).
9. A. Waldbaur, B. Waterkotte, K. Schmitz, and B. E. Rapp, "Maskless projection lithography for the fast and flexible generation of grayscale protein patterns," Small **8**, 1570–1578 (2012).
10. K. Totsu, K. Fujishiro, S. Tanaka, and M. Esashi, "Fabrication of three-dimensional microstructure using maskless gray-scale lithography," Sens. Actuat. A, Phys. **130**, 387–392 (2006).
11. B. Yang, J. Zhou, Q. Chen, L. Lei, and K. Wen, "Fabrication of hexagonal compound eye microlens array using DMD-based lithography with dose modulation," Opt. Express **26**, 28927–28937 (2018).
12. X. Ma, Y. Kato, F. van Kempen, Y. Hirai, T. Tsuchiya, F. van Keulen, and O. Tabata, "Experimental study of numerical optimization for 3-D microstructuring using DMD-based grayscale lithography," J. Microelectromech. Syst. **24**, 1856–1867 (2015).
13. Z. Zhang, Y. Gao, N. Luo, and K. Zhong, "Fast fabrication of curved microlens array using DMD-based lithography," AIP Adv. **6**, 015319 (2016).
14. Q. Deng, Y. Yang, H. Gao, Y. Zhou, Y. He, and S. Hu, "Fabrication of micro-optics elements with arbitrary surface profiles based on one-step maskless grayscale lithography," Micromachines **8**, 314 (2017).
15. S. Huang, M. Li, L. Shen, J. Qiu, and Y. Zhou, "Fabrication of high quality aspheric microlens array by dose-modulated lithography and surface thermal reflow," Opt. Laser Technol. **100**, 298–303 (2018).
16. R. He, S. Wang, G. Andrews, W. Shi, and Y. Liu, "Generation of customizable micro-wavy pattern through grayscale direct image lithography," Sci. Rep. **6**, 21621 (2016).
17. C. Sun, N. Fang, D. M. Wu, and X. Zhang, "Projection micro-stereolithography using digital micro-mirror dynamic mask," Sens. Actuat. A, Phys. **121**, 113–120 (2005).
18. S. Song, K. Kim, S. Choi, S. Han, H. Lee, S. Kwon, and W. Park, "Fine-tuned grayscale optofluidic maskless lithography for three-dimensional freeform shape microstructure fabrication," Opt. Lett. **39**, 5162–5165 (2014).
19. J. Kim, S. Chung, S. Choi, H. Lee, J. Kim, and S. Kwon, "Programming magnetic anisotropy in polymeric microactuators," Nat. Mater. **10**, 747–752 (2011).
20. S. Habasaki, W. Lee, S. Yoshida, and S. Takeuchi, "Vertical flow lithography for fabrication of 3D anisotropic particles," Small **11**, 6391–6396 (2015).
21. R. He, D. Yunus, C. Uhl, W. Shi, S. Sohrabi, and Y. Liu, "Fabrication of circular microfluidic channels through grayscale dual-projection lithography," Microfluid. Nanofluid. **21**, 13 (2017).
22. J. Na, N. P. Bende, J. Bae, C. D. Santangelo, and R. C. Hayward, "Grayscale gel lithography for programmed buckling of non-Euclidean hydrogel plates," Soft Matter **12**, 4985–4990 (2016).
23. W. Chen, S. Kirihara, and Y. Miyamoto, "Fabrication and measurement of micro three-dimensional photonic crystals of SiO_2 ceramic for terahertz wave applications," J. Am. Ceram. Soc. **90**, 2078–2081 (2007).
24. H. Kim, J. Ge, J. Kim, S. Choi, H. Lee, H. Lee, W. Park, Y. Yin, and S. Kwon, "Structural colour printing using a magnetically tunable and lithographically fixable photonic crystal," Nat. Photonics **3**, 534–540 (2009).
25. H. Lee, J. Kim, H. Kim, J. Kim, and S. Kwon, "Colour-barcoded magnetic microparticles for multiplexed bioassays," Nat. Mater. **9**, 745–749 (2010).
26. P. Zhang, Q. Zhang, J. Zeng, J. Han, J. Zhou, W. Zhang, Q. Jiao, Y. Wu, and S. Dai, "Fabrication of planar photonic crystals in chalcogenide glass film by maskless projection lithography," Appl. Phys. B **122**, 244 (2016).
27. D. J. Heath, B. Mills, M. Feinaeugle, and R. W. Eason, "Rapid bespoke laser ablation of variable period grating structures using a digital micromirror device for multi-colored surface images," Appl. Opt. **54**, 4984–4988 (2015).
28. Q. Li, M. Ji, and J. Kim, "Grayscale nanopixel printing at sub-10-nanometer vertical resolution via light-controlled nanocapillarity," ACS Nano **14**, 6058–6066 (2020).
29. R. Negishi, K. Takai, T. Tanaka, T. Matsunaga, and T. Yoshino, "High-throughput manipulation of circulating tumor cells using a multiple single-cell encapsulation system with a digital micromirror device," Anal. Chem. **90**, 9734–9741 (2018).
30. G. Brooker, *Modern Classical Optics* (Oxford University, 2003).
31. Y. Park, S. Kim, C. Moon, and H. Jeon, "Butt-end fiber coupling to a surface-emitting Γ-point photonic crystal bandedge laser," Appl. Phys. Lett. **90**, 171115 (2007).
32. W. Han, W. Cheng, and Q. Zhan, "Design and alignment strategies of 4f systems used in the vectorial optical field generator," Appl. Opt. **54**, 2275–2278 (2015).
33. S. Kim, J. Lee, and H. Jeon, "Over 1 hour continuous-wave operation of photonic crystal lasers," Opt. Express **19**, 1–6 (2011).
34. H.-J. Thiele and M. Nebeling, eds., *Coarse Wavelength Division Multiplexing: Technologies and Applications* (CRC Press, 2007).
35. J. Yoon, K. Kim, and W. Park, "Modulated grayscale UV pattern for uniform photopolymerization based on a digital micromirror device system," Appl. Phys. Lett. **111**, 033505 (2017).
36. Q. Li, Y. Xiao, H. Liu, H. Zhang, J. Xu, and J. Li, "Analysis and correction of the distortion error in a DMD based scanning lithography system," Opt. Commun. **434**, 1–6 (2019).
37. Z. Shi and Y. Gao, "Fast imaging algorithm for DMD-based photolithography with partially coherent illumination," Optik **123**, 1640–1645 (2012).

38. J. Liu, J. Liu, Q. Deng, J. Feng, S. Zhou, and S. Hu, "Intensity modulation based optical proximity optimization for the maskless lithography," Opt. Express **28**, 548–557 (2020).
39. N. Werth, M. S. Muller, J. Meier, and A. W. Koch, "Diffraction errors in micromirror-array based wavefront generation," Opt. Commun. **284**, 2317–2322 (2011).
40. K. Chan, Z. Feng, R. Yang, A. Ishikawa, and W. Mei, "High-resolution maskless lithography," J. Microlith. Microfab. Microsyst. **2**, 331 (2003).
41. K. Kim, S. Han, J. Yoon, S. Kwon, H. Park, and W. Park, "Lithographic resolution enhancement of a maskless lithography system based on a wobulation technique for flow lithography," Appl. Phys. Lett. **109**, 234101 (2016).
42. R. Chen, H. Liu, H. Zhang, W. Zhang, J. Xu, W. Xu, and J. Li, "Edge smoothness enhancement in DMD scanning lithography system based on a wobulation technique," Opt. Express **25**, 21958–21968 (2017).
43. C. Peng, Z. Zhang, J. Zou, and W. Chi, "A high-speed exposure method for digital micromirror device scanning maskless lithography system," Optik **185**, 1036–1044 (2019).
44. Y. Zhang, J. Luo, Z. Xiong, H. Liu, L. Wang, Y. Gu, Z. Lu, J. Li, and J. Huang, "User-defined microstructures array fabricated by DMD based multistep lithography with dose modulation," Opt. Express **27**, 31956–31966 (2019).